Henry G. Roe,[2]

***PASP*, in press.**

ABSTRACT

Many adaptive optics systems operate by measuring the distortion of the wavefront in one wavelength range and performing the scientific observations in a second, different wavelength range. One common technique is to measure wavefront distortions at wavelengths $<\sim 1$ μm while operating the science instrument at wavelengths $>\sim 1$ μm. The index of refraction of air decreases sharply from shorter visible wavelengths to near-infrared wavelengths. Therefore, because the adaptive optics system is measuring the wavefront distortion in one wavelength range and the science observations are performed at a different wavelength range, residual image motion occurs and the maximum exposure time before smearing of the image can be significantly limited. We demonstrate the importance of atmospheric differential refraction, present calculations to predict the effect of atmospheric differential refraction, and finally discuss the implications of atmospheric differential refraction for several current and proposed observatories.

Subject headings: atmospheric effects — instrumentation: adaptive optics

1. Introduction

Adaptive Optics (AO) has been used for astronomical observations for more than a decade and numerous medium-to-large telescopes around the world are now equipped with AO systems. If an AO system's wavefront sensor operates at different wavelengths than are being observed by the science instrument, and no correction is made for atmospheric differential refraction, the target object will appear to drift with respect to the science instrument. An example of the problem this phenomenon can introduce is shown in Fig. 1 which is the difference of two images of Saturn's moon Titan taken just 2.5 minutes apart while continuously tracking and correcting on Titan with the Keck II telescope's AO system. The maximum exposure time possible without degrading the spatial resolution of the data is significantly restricted if no correction for atmospheric differential refraction is made.

Adaptive optics systems for astronomical observing operate by splitting the incoming light into two beams, one of which goes to the wavefront sensor of the AO system and the goes to the science instrument. In many cases a dichroic optic is used as the beamsplitter in order to send visible light ($<\sim 1\mu$m) to the wavefront sensor and infrared light ($>\sim 1\mu$m) to the science instrument. Examples of telescopes with AO systems that can operate in this way include the 3-m Shane telescope at Lick Observatory (Gavel et al. 2000), the CFHT 3.6-m telescope (Rigaut et al. 1998), the Gemini North 8-m telescope (Graves et al. 2000), and

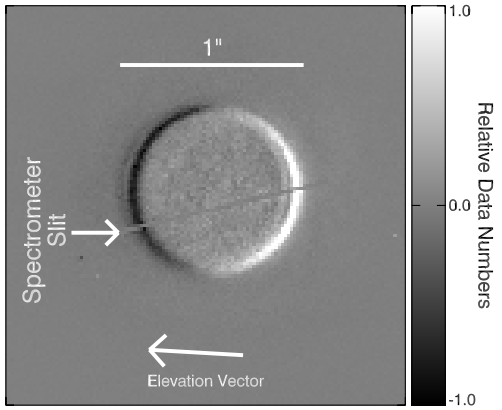

Fig. 1.— The difference between two raw images of Titan taken just 153 seconds apart with NIRSPEC's SCAM detector on the Keck II telescope while continuously guiding/correcting with the AO system on Titan. Each image is the result of three 10 second exposures. At the start of the first sequence of exposures Titan was at an elevation of 57.°86 and an hour angle of 2.25; 153 seconds later when the second set of exposures started Titan was at an elevation of 57.°26. Titan's declination was 16.°73. The 1-pixel wide slit of NIRSPEC's spectrometer is across Titan's disk and the apparent motion of Titan due to the effect of atmospheric differential refraction is obvious along the elevation vector.

[1]Data presented herein were obtained at the W.M. Keck Observatory, which is operated as a scientific partnership among the California Institute of Technology, the University of California, and the National Aeronautics and Space Administration. The Observatory was made possible by the generous financial support of the W.M. Keck Foundation.

[2]Department of Astronomy, 601 Campbell Hall, University of California, Berkeley, CA 94720-3411. (*hroe@astro.berkeley.edu*)

both of the W.M. Keck Observatory's 10-m telescopes (Wizinowich et al. 2000). The wavefront sensor measures the distortions to the wavefront and a correction is calculated and applied to a deformable mirror. The first order of distortion that an AO system is called upon to correct is simply image motion, commonly known as 'tip/tilt'. If significant tip/tilt residuals remain after AO correction then the resulting data will be of lower spatial resolution, regardless of how well the AO system corrects for the higher order terms of focus, astigmatism, coma, and so forth. Minimizing tip/tilt residuals is critical to achieving optimum performance from an AO system. The effect of atmospheric differential refraction is to introduce a systematic tip/tilt error that an AO system will not correct for unless specifically accounted for in the AO control software. For ease in the remainder of this report we will refer to atmospheric differential refraction as "ADR".

Problems due to ADR arise when the AO system is correcting on visible wavelength light and the science instrument is observing at infrared wavelengths. From visible to infrared wavelengths the refractive index of air decreases sharply, as shown in Fig. 2. A star's visible pointing center always appears at higher elevation than a star's infrared pointing center, except when the star is at the zenith. That the two pointing centers do not coincide is not unto itself a problem for the typical AO system, however the offset between the two pointing centers is not constant. Without some consideration for the effect of ADR, a properly performing AO system will hold the visible pointing center of the star fixed, relative to both the wavefront sensor and the science camera. However as time progresses and the star moves in elevation, the infrared pointing center will drift with respect to the visible pointing center, and thus in the infrared the star appears to drift with respect to the science instrument. Observers must consider this effect in determining the maximum exposure times in order to avoid 'trailed' images, unless some other compensation is made.

In this paper we present calculations demonstrating when and how much of a problem ADR can be for an AO system. Using data taken with the AO system on the Keck II telescope we show that in a long exposure, or sequence of exposures, the most significant uncorrected tip-tilt motion is due to the effect of ADR. We further show that the effect of ADR is dependent on the spectral type, or color, of the star being used as a reference source. Finally, we discuss the implications of ADR for AO observing with current and currently proposed telescopes. The code used in these calculations is available with the electronic version of this paper or by request from the author. While the code is written in the commonly used IDL programming language, it could easily be translated to other languages. We encourage others to investigate the implications of ADR for their favourite telescope, site, target, observing strategy, etc..

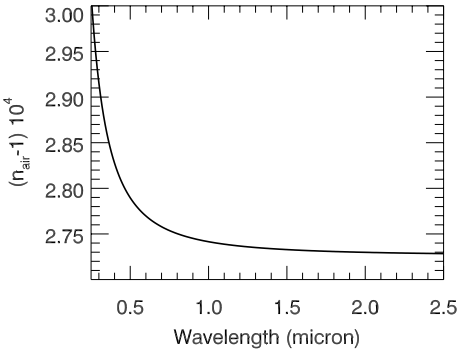

Fig. 2.— The refractive index of air as a function of wavelength across the visible and near-infrared spectrum at standard temperature and pressure in the absence of water vapor.

2. Theoretical Calculations

The equations necessary for calculating the effect of ADR are given by Schubert & Walterscheid (2000). From Schubert & Walterscheid (2000) the refractive index of air n at pressure p millibar, temperature T Kelvin, partial pressure of water vapor p_w millibar[3], and wavelength λ microns is

$$n\left(\lambda, p, T, p_w\right) = 1+ \left[64.328 + \frac{29498.1}{146-\lambda^{-2}} + \frac{255.4}{41-\lambda^{-2}}\right]\left[\frac{pT_s}{p_s T}\right]10^{-6} - 43.49\left[1 - \frac{7.956\times10^{-3}}{\lambda^2}\right]\frac{p_w}{p_s}10^{-6}, \quad (1)$$

where p_s is 1013.25 millibar and T_s is 288.15 K. For a given refractive index n the angle between the true zenith distance z_t and the apparent zenith distance z_a is well approximated by

$$R \equiv z_t - z_a \simeq 206265\left(\frac{n^2-1}{2n^2}\right)\tan z_t \quad \text{arcsec} \quad (2)$$

[3]Schubert & Walterscheid (2000) contains a typo that resulted in a missing factor of 10^{-6} for the water vapor correction. Equation 2 here is correct.

for zenith distances less than about 80°. Observers typically work at much more modest zenith distances of $z_t < 40° - 50°$ where this approximation is extremely good.

Atmospheric differential refraction between two wavelengths (e.g. λ_{vis} of an AO wavefront sensor and λ_{ir} of a science instrument) is then

$$R_{vis} - R_{ir} = 206265 \left(\frac{n_{vis}^2 - 1}{2n_{vis}^2} - \frac{n_{ir}^2 - 1}{2n_{ir}^2} \right) \tan z_t \quad \text{arcsec} \tag{3}$$

Note that equation 4 is written to give a positive angular distance since the zenith distance of the visible pointing center, z_{vis}, will be less than that of the infrared pointing center, z_{ir}. The true zenith distance (z_t) is related to latitude of the observer (ϕ), declination of the target (δ), and hour angle of the target (H) by

$$\cos(z_t) = \sin(\phi)\sin(\delta) + \cos(\phi)\cos(\delta)\cos(H) \tag{4}$$

To relate the ADR offset of equation 4 to the (x,y) coordinates of a detector array oriented arbitrarily with respect to the sky, we introduce several angles. As shown in Fig. 3 the parallactic angle ($ParAng$) is the angle from the sky North vector counter-clockwise to the elevation-up vector. Position angle ($PosAng$) is the angle from the increasing Y-direction of the detector array clockwise to the sky North vector. Finally, the difference of PosAng minus ParAng gives the angle from the increasing Y-direction clockwise to the elevation up vector. In the (x,y) coordinates of the detector array the offset from visible pointing center to infrared pointing center is then

$$X_{offset} = \frac{R_{ir} - R_{vis}}{PlateScale} \sin(PosAng - ParAng) \tag{5}$$

$$Y_{offset} = \frac{R_{ir} - R_{vis}}{PlateScale} \cos(PosAng - ParAng), \tag{6}$$

where $PlateScale$ is arcseconds per pixel of the array. The parallactic angle ($ParAng$) is a function of hour angle, declination, and latitude,

$$\tan(ParAng) = \frac{\sin(H)}{\cos(\delta)\tan(\phi) - \sin(\delta)\cos(H)}. \tag{7}$$

In the coordinate system of elevation and azimuth, the motion of the infrared pointing center relative to the visible pointing center due to ADR is always along the elevation vector. However, most observations are made using a field rotator

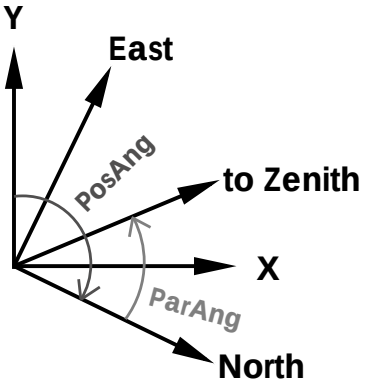

Fig. 3.— Schematic clarifying definition of position angle and parallactic angle. The parallactic angle ($ParAng$) is defined as the angle measured from the vector pointing north on the sky counter-clockwise to the vector pointing to the zenith. The position angle ($PosAng$) is defined as the angle measured from the positive Y-direction on the detector array clockwise to the vector pointing north on the sky.

such that instrument coordinates remain fixed relative to right ascension and declination. Therefore the instrument coordinate system rotates relative to elevation and azimuth. The important point is that the instrument coordinate system rotates about the visible pointing center. Thus, the effective motion of the infrared pointing center in instrument coordinates is not along the elevation vector except when the parallactic angle is unchanging. In the images of Titan differenced in Fig. 1 the parallactic angle was nearly unchanging and therefore the motion due to ADR appears along the elevation vector. In later examples the parallactic angle is changing rapidly and then the apparent motion is not along the elevation vector.

Equation 4 gives the instantaneous offset between visible and infrared pointing centers, but it is the first derivative of $R_{ir} - R_{vis}$ with respect to time that causes the problem addressed in this paper. In the extreme case of an AO equipped telescope at the South Pole, ADR, as described in this current report, is not a problem since targets do not move in elevation angle.

In order to find the instantaneous rate of image motion due to ADR we define the constant

$$\beta = \frac{206265}{PlateScale} \left(\frac{n_{ir}^2 - 1}{2n_{ir}^2} - \frac{n_{vis}^2 - 1}{2n_{vis}^2} \right) \tag{8}$$

and take the partial derivative of X_{offset} and Y_{offset} with respect to hour angle.

$$\frac{\partial}{\partial H} X_{offset} = \beta \sin\left(PosAng - ParAng\right) \sec^2\left(z_t\right) \frac{\partial z_t}{\partial H} - \beta \tan\left(z_t\right) \cos\left(PosAng - ParAng\right) \frac{\partial ParAng}{\partial H} \quad (9)$$

$$\frac{\partial}{\partial H} Y_{offset} = \beta \cos\left(PosAng - ParAng\right) \sec^2\left(z_t\right) \frac{\partial z_t}{\partial H} + \beta \tan\left(z_t\right) \sin\left(PosAng - ParAng\right) \frac{\partial ParAng}{\partial H} \quad (10)$$

The partial derivatives of z_t and $ParAng$ with respect to H are

$$\frac{\partial}{\partial H} z_t = \frac{\cos\left(\delta\right) \cos\left(\phi\right) \sin\left(H\right)}{\sqrt{1 - \left(\cos\left(H\right) \cos\left(\delta\right) \cos\left(\phi\right) + \sin\left(\delta\right) \sin\left(\phi\right)\right)^2}} \quad (11)$$

$$\frac{\partial}{\partial H} ParAng = \frac{\cos\left(H\right) \cos\left(\delta\right) \tan\left(\phi\right) - \sin\left(\delta\right)}{\sin^2\left(H\right) + \left(\cos\left(H\right) \sin\left(\delta\right) - \cos\left(\delta\right) \tan\left(\phi\right)\right)^2} \quad (12)$$

The combination of eqns. 8, 12, and 13 with

$$\frac{d}{dt} H = \frac{\pi \text{ radian}}{1800 \text{ minute}} \quad (13)$$

into eqns. 10 and 11 gives the instantaneous rate of image motion in the x/y-plane of the detector. The IDL routine *adr_rateofmotion.pro* included in the electronic version of this paper calculates this instantaneous rate of image motion.

Finding the maximum exposure time allowed before the image motion exceeds some given limit is not as straightforward as simply dividing the desired image motion limit by the instantaneous rate of image motion at the start of the exposure. This is because the image motion is usually curved in the x/y-plane and because the second partial derivatives of X_{offset} and Y_{offset} with respect to time are not constants. Therefore, the most direct method of determining the maximum exposure time is to calculate X_{offset} and Y_{offset} with fine time sampling and simply search for the point at which the maximum desired image motion has been exceeded. The IDL routine *adr_maxexptime.pro*, included in the electronic version of this paper, calculates the maximum allowed exposure time.

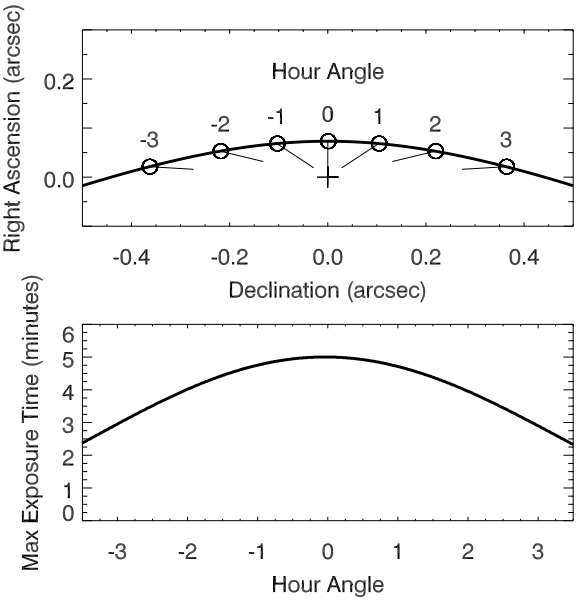

Fig. 4.— (a) predicted image motion and (b) maximum exposure times for an observation at 1.65 μm (H-band) of a target at declination +30° with the Keck 10-meter telescope assuming an effective wavelength of 0.65 μm for the wavefront sensor of the AO system. Each hour angle is marked by a circle and a line pointing toward the zenith at that moment. The motion due to ADR is not necessarily along the elevation vector. Note that (a) does not depend on telescope aperture, but does depend on wavelengths of observation, declination of target, and latitude of observatory. The origin of the coordinate system in (a) lies at the visible wavelength pointing center, which the AO system is holding steady. Maximum exposure time in (b) is calculated for a 10-meter diameter telescope and assuming maximum allowed image motion of 0.25 of the FWHM of the diffraction limited point spread function.

Output from these calculations for an observation with the Keck telescope is shown in Fig. 4. The predicted motion shown in Fig. 4a depends on site, but not diameter of telescope, while the maximum exposure times shown in Fig. 4b are based on the 10-meter diameter of the Keck telescopes. A smaller telescope has a coarser diffraction limit and therefore is less affected by the issue of drift due to differential refraction, however some smaller telescopes are at lower sites (e.g. the Shane 3-m of Lick Observatory) where differential refraction is greater. A smaller telescope at a higher altitude, higher latitude site suffers less from ADR than a larger telescope at a lower altitude, lower latitude site. The implications of ADR for several current and proposed telescopes are discussed in section 4.

A critical parameter in calculating the implications of ADR is the effective wavelength of the reference source on the wavefront sensor. The wavefront sensor of an AO system is often photon limited and therefore designed to have as broad a wavelength bandpass as possible. In the case of a broad wavefront sensor bandpass, the effective wavelength of the reference source on the wavefront sensor depends on the color of source, as we will show in section 3 using observed data. Usually of less importance is the effective wavelength of the target on the science instrument since the variation of air's refractive index with wavelength is much less in the near-infrared than in the visible.

3. Data Reduction and Analysis

All the data presented here were taken using the W.M. Keck Observatory's near-infrared spectrograph NIRSPEC behind the AO system on the Keck II 10-meter telescope. NIRSPEC contains two infrared arrays: a 1024 × 1024 InSb ALADDIN for spectroscopy and a 256 × 256 HgCdTe PICNIC array as a slit-viewing camera (SCAM). The images of Titan shown in Fig. 1 were taken 2001 January 11 (UT) during high-spectral resolution long-exposure spectroscopy for a project of Eliot Young's. This observing run was the first time we noticed the problems presented by atmospheric differential refraction when observing with AO. The images shown in Fig. 1 are 30-second exposures taken just 2.5 minutes apart and clearly show a movement of ∼1 pixel, or ∼1/2 the full width at half maximum (fwhm) of the diffraction limit.

During the nights of 2001 August 20 and 21 (UT) James Lloyd and James Graham observed several binary stars as part of an ongoing search for low-mass companions. Images were taken of each field nearly continuously for 30 to 60 minutes while neither adjusting the parameters of the AO system nor offsetting the pointing of the telescope. We first discuss platescale and position angle calibration using several Hipparcos binary star systems. We then focus on data on two of Lloyd & Graham's stars (HIP 110 and HIP 13117) to show that on multi-minute time scales atmospheric differential refraction is the dominant image blurring effect that is uncorrected by the AO system. Further, we use these data to show that the spectral type or color of the star is important when considering how to correct for ADR.

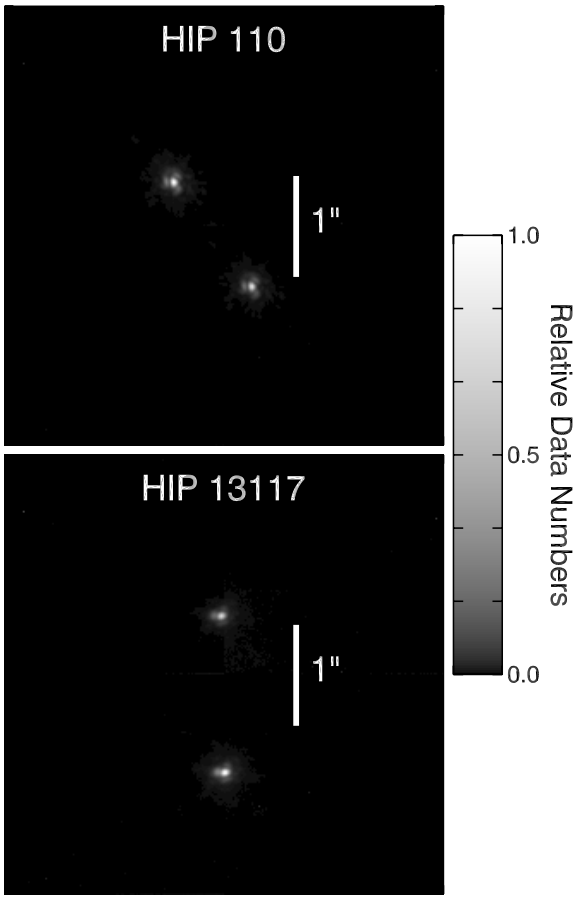

Fig. 5.— Example images of HIP 110 and HIP 13117. These images have been processed using standard near-infrared techniques of sky-subtraction and flat-fielding. Bad pixels have been replaced with the median of their nearest 4 to 8 good neighbors.

3.1. Calibration of Platescale and Position Angle

The platescale of SCAM behind AO was designed to well sample the core of a diffraction limited point spread function (PSF) in the near-infrared with a pixel size of approximately 0.″017. In order to determine the true platescale of SCAM behind AO and confirm the accuracy of the instrument-reported position angle, four Hipparcos binary systems chosen for their small uncertainty in separation and small parallax were observed earlier on the evenings of 2001 August 20 and 21 (UT) by de Pater *et al.*. The details of these plate scale calibrations are given in Table 1. Each Hipparcos field was imaged at a number of positions around SCAM's field-of-view in order to check for distortions. As noted in Table 1, three of the four fields were imaged a second time after a 90° rotation of SCAM's field-of-view. All

TABLE 1
DETAILS OF PLATE-SCALE CALIBRATION.

Star Name	# of images	Coadds× Exposure Time	Assumed P.A. of Binary[a]	SCAM Reported P.A.[b]	Measured P.A.[c]	Hipparcos Binary Separation	Measured Separation (pixels)	Derived Plate Scale (mas/pixel)
HIP 83634	14	10×0.1 s	306.°4	92.°0	92.°13±0.°23	1.″436±0.″007	87.03±0.51	16.50±0.013
HIP 83634	17	10×0.1 s	306.°4	2.°0	1.°95±0.°29	1.″436±0.″007	87.24±0.49	16.46±0.012
HIP 89947	6	50×0.2 s	340.°1	92.°0	92.°33±0.°53	1.″642±0.″006	98.67±0.30	16.64±0.008
HIP 91362	10	50×0.2 s	223.°2	82.°0	82.°63±0.°35	1.″050±0.″009	61.88±0.52	16.97±0.020
HIP 91362	10	50×0.2 s	223.°2	-8.°0	-7.°21±0.°34	1.″050±0.″009	62.29±0.31	16.86±0.017
HIP 100847	10	10×1.0 s	129.°	-8.°0	-8.°28±0.°24	0.″871±0.″010	51.59±0.23	16.88±0.021
HIP 100847	10	10×1.0 s	129.°	-98.°0	-97.°87±0.°55	0.″871±0.″010	51.93±0.36	16.77±0.022

[a]Position angle of secondary star relative to primary star as reported in the Hipparcos catalog (ESA 1997).

[b]Position angle of the SCAM detector reported by the instrument hardware. See Fig. 3 for definition.

[c]Position angle of the SCAM detector determined from the data assuming the position angle of the binary pair given in ESA (1997) is perfect.

of these data were taken in the H-band filter and were processed using standard infrared techniques of sky subtraction and flat-field correction using data taken on the twilight sky. To measure the x,y offset between two stars on the same image we rebinned the image by a factor of 8 (64 new pixels for each original pixel) using sampling and then calculated the autocorrelation function

$$\mathbf{A} = \mathrm{FFT}^{-1}\left(\mathrm{FFT}\left(\mathbf{R}\right)\mathrm{Conjugate}\left(\mathrm{FFT}\left(\mathbf{R}\right)\right)\right), \quad (14)$$

where $\mathbf{R}$ is the rebinned image, FFT represents a forward fast fourier transform, and FFT^{-1} represents an inverse fast fourier transform. The position of the secondary maxima in $\mathbf{A}$ gives the x,y offset between the two stars. Table 1 gives the Hipparcos measured position angle (PA) of each binary pair, the PA of the detector as reported by the instrument hardware, and the PA of the detector measured from the data assuming no motion of the stars since the epoch of the Hipparcos observations. Further, Table 1 gives the Hipparcos measurement of angular separation for each pair, our measured separation in pixels, and the implied plate scale for our detector. For the current work we adopt a plate scale of 0.″0167±0.″0002 per pixel, although we note that most of the uncertainty in this determination of plate scale appears to be due to inaccuracies in the 'known' separation of the binaries in the Hipparcos catalog, suggesting that these binaries have moved slightly in separation since the epoch of Hipparcos (1991.25). The position angle determination shown in Table 1 demonstrates that the instrument-reported position angle is accurate to better than $\sim 0.°5$.

3.2. Measurement of Differential Refraction

The relevant ephemeris data and details of the observations of HIP 110 and HIP 13117 are shown in Tables 2 and 3. Note that two separate sequences of data were taken on HIP 110. All of the stellar data were taken in the K-prime filter, each image containing 100 coadds of 0.40 second exposure. Each pair of binary stars were aligned on the chip to avoid regions of bad pixels. The images were processed using standard infrared techniques of bias subtraction and flat-field correction using data taken on the twilight sky. Those pixels that were flagged as bad were replaced with the median of their nearest 4-8 good neighbors. Example frames from both fields are shown in Fig. 5.

The goal of this exercise is to track the motion of a star across the several dozen images that make up an exposure sequence. To do this we extract a region of roughly ±50 pixels around the star from each image of the sequence. In essence we then oversample by a factor of 4 and find the peak of the cross-correlation function for every pair of images in this extracted stack. From this matrix of

TABLE 2
BINARY STARS USED FOR FITTING FOR THE EFFECTS OF ADR.

Star	m_V	Parallax (milliarcsec)	$B-V$[a]	$V-I$[a]	ΔHIPmag[a,b]	Separation[a] (arcsec)	Spectral Type[c]
HIP 110	8.61	20.42±1.91	0.787±0.003	0.820±0.007	0.64±0.03	1.197	GV
HIP 13117	11.69	29.67±9.34	1.460±0.022	1.85±0.10	0.64±0.22	1.679	MV

[a]From the Hipparcos catalog (ESA 1997).

[b]Magnitude difference between the two stars of the binary in the ESA (1997) defined passband.

[c]Spectral type and class estimated from the tables of Drilling & Landolt (2000) using m_V, parallax, $B-V$, and $V-I$.

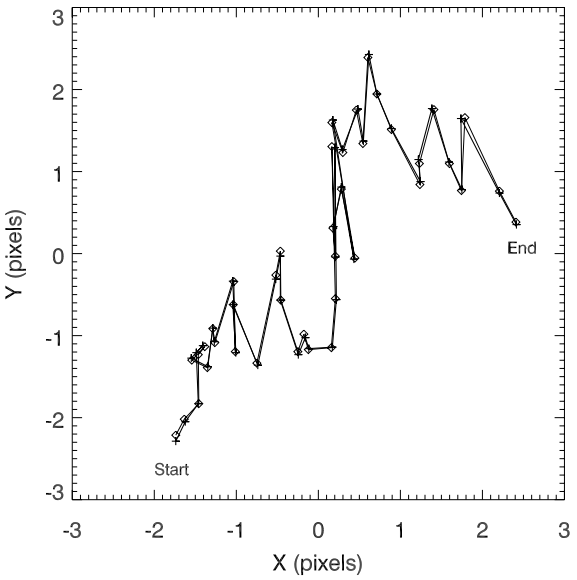

Fig. 6.— Image motion during second sequence of HIP 110 observations as derived independently from each component of the HIP 110 binary.

quarter-pixel resolution offsets between every pair of images we calculate a least-squares fit for the relative offsets of the images. Since each field contains two stars we can do this for each star and obtain an internal cross-check on our method of tracking image motion. Figure 6 shows the image motion during the second sequence of HIP 110 observations as measured from each of the components of HIP 110, which agree well with each other. This good agreement gives us confidence that our method of detecting image motion is not affected by issues such as bad pixels, residual flat-field noise, read-noise, etc. that would differ between the two stars.

For each of the six observed sequences (2 components of HIP 110 observed in two separate sequences and 2 components of HIP 13117) we use the downhill simplex method 'amoeba' of Press, Teukolsky, Vetterling, & Flannery (1992) as implemented in the IDL software package to fit for the effect of ADR. The fixed parameters are: the zenith distance of each observation, the parallactic angle of each observation, the relative (x,y) offset of each observation, the platescale, the position angle of the SCAM array, the atmospheric pressure and temperature, the partial pressure of atmospheric water vapor, and the effective wavelength of the star on SCAM. The parameter of interest being fit for is the effective wavelength of the reference star on the wavefront sensor. Also allowed to vary is the (x,y) position where the star would appear on SCAM at the effective wavelength of the wavefront sensor. This (x,y) position is constant within an observing sequence. The results of these fits are shown with their corresponding observations in Fig. 7 and are summarized in Table 3. For the purposes of this fitting we assumed a typical atmospheric pressure and temperature for Mauna Kea of 456 mm Hg and 2°C (Cohen & Cromer 1988). We also assumed a water vapor partial pressure of zero, although we found no variation in our results over a reasonable range of water vapor partial pressures for the summit of Mauna Kea.

A thorough examination of the uncertainties in our determination of effective wavelength on the wavefront sensor is difficult, primarily because the

residuals of the fits (dashed lines in Fig. 7) are clearly not randomly distributed. While most of the residual image motion is attributable to ADR, there appear to be other phenomena causing residual image motion at the several pixel level.

One method for better understanding the uncertainties in best-fit λ_{eff} is to refit λ_{eff} to a randomly chosen fraction of the observations. For each observational sequence we randomly chose one half of the observations and refit for λ_{eff}. By repeating this procedure 1000 times for each observational sequence we made the error estimates shown in Table 3. The major source of systematic uncertainty in λ_{eff} is the uncertainty in platescale, which adds an additional ± 0.004 μm uncertainty to the values of λ_{eff} in Table 3. This is not a truly rigorous exercise in error analysis, however it does show that the uncertainties in λ_{eff} for HIP 110 and HIP 13117 ($\sim< 0.025$ μm) are

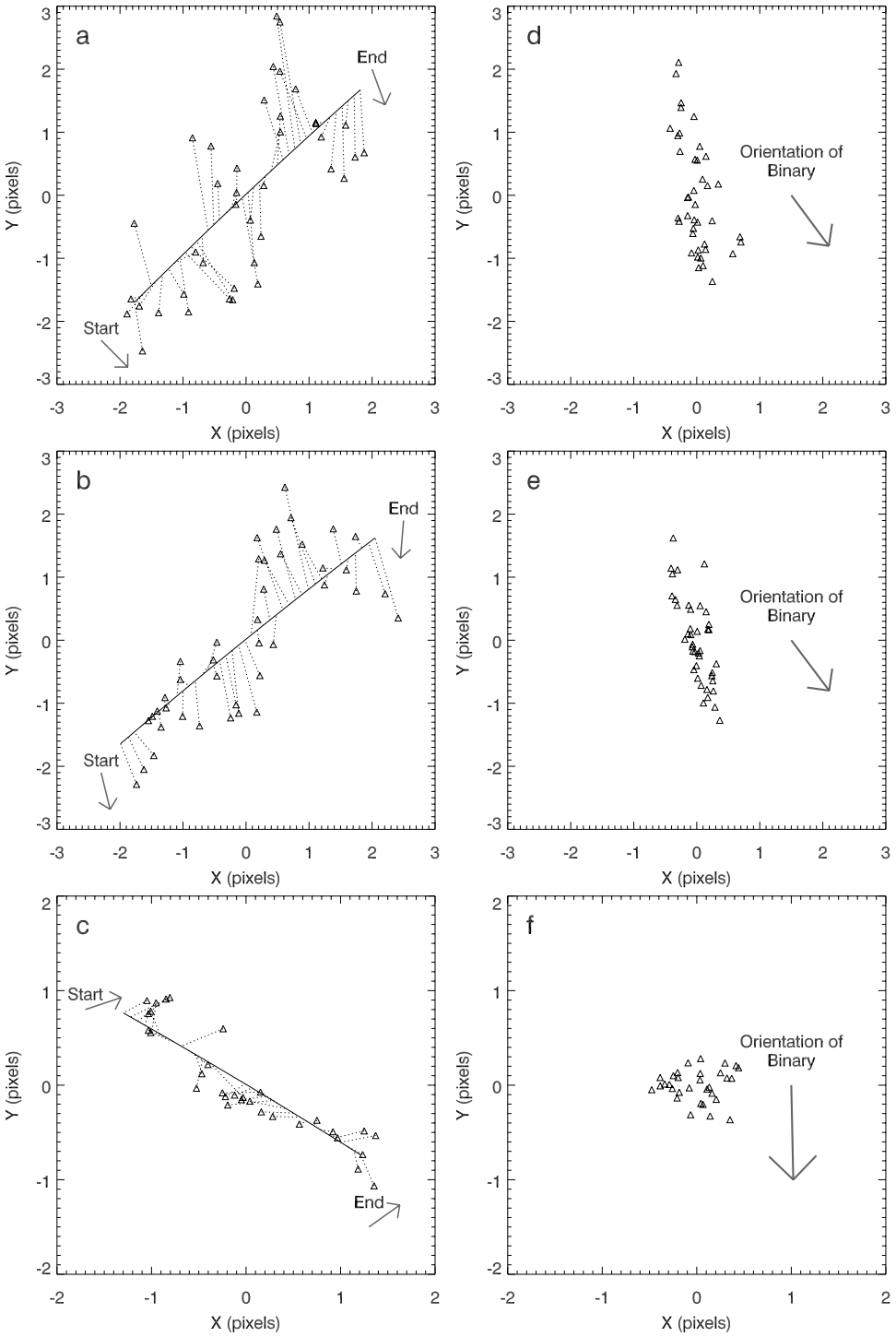

Fig. 7.— Image motion for the brighter component of each binary pair. (a) is the first sequence of HIP 110 observations, (b) is the second sequence of HIP 110, and (c) is HIP 13117. The triangles mark the relative positions of the star from image to image. The solid line is the best-fit for the motion due to ADR. The dashed lines connect each observation (triangle) with its corresponding point along the best-fit solid line. As shown in Fig. 6 the image motion derived from each binary component is nearly identical and therefore the fits to the secondary components are not shown in this figure, but the resulting best-fit effective wavelengths are included in Table 3. Also shown on (a), (b), and (c) are gray arrows pointing to the zenith at the start and end of each sequence of observations. (d), (e), and (f) show the image motion residuals of the observations in (a), (b), and (c) after subtracting the motion due to ADR. Note the asymmetry of the residuals in the case of HIP110 in (d) and (e). This is due to the close separation of HIP110 influencing the AO correction as described in the text. The orientation of the binary pair in each observation sequence is indicated by an arrow.

much less than the difference between λ_{eff} for HIP 110 and HIP 13117 (~ 0.11 μm). As expected, we find that HIP 13117, an MV star, has a redder λ_{eff} than HIP 110, which is a GV star. Our detection of the color difference between these two stars is real and shows that to fully correct for the effect of ADR the color of the AO calibrator source must be taken into account.

Figure 7 shows that the largest source of residual image motion is accounted for by ADR, however residuals of up to 1 to 2 pixels ($0\farcs017 - -0\farcs034$) remain, which are significant given that the diffraction limit resolution is $0\farcs046$ at 2.15 μm. The source of the largest remaining residuals is most likely due to the binary nature of these stars. The AO system uses light from the brighter of the two stars to measure the wavefront distortion. In these observations a 1" field stop is employed in front of the wavefront sensor in order to block the light of the dimmer star from reaching the sensor. With binaries of closer separation, moments of worse seeing can cause light from the dimmer star to leak in through the field stop. During these moments the AO correction is worse and the residual tip-tilt error in the direction of the position angle of the binary will be larger. In support of this argument that the larger tip-tilt residuals we observe are due to this binary effect, we show in Fig. 7d-f the residuals of tip-tilt image motion after subtracting the effect of ADR. For both observations of HIP110 these residuals are extremely asymmetrical in the x-y plane, with the larger residuals parallel to the position angle of HIP110. In these data the position angle of HIP110 is approximately orthogonal to the direction of motion due to ADR. The residuals in the direction of motion due to ADR are approximately gaussian distributed with $\sigma = 0.3$ pixels. The stars of HIP13117 are more widely separated and thus the AO correction is less affected by this binary star issue. This is apparent in that the residuals of image motion measured for HIP13117 are roughly symmetrically distributed in the x-y plane with a standard deviation of 0.3 pixels.

4. Implications for Observing

Ideally one would know λ_{eff} of the reference source on the WFS and λ_{eff} of the science target on the science instrument. The AO system could then continuously correct for the calculated effect of differential refraction by inserting tip-tilt motions in order to keep the science target steady on the science instrument. Some AO systems have implemented this type of correction. However, in some cases for practical reasons implementing this correction may be difficult, or λ_{eff} of the reference source on the wave-front sensor may not be well known. Knowing λ_{eff} of the science target on the science instrument is less critical since the index of refraction of air varies much more gradually at near-infrared wavelengths than visible wavelengths. In the following sections we investigate both of these cases for several existing and proposed telescopes. An alternative technique for ADR correction is to insert an atmospheric dispersion corrector between the telescope and AO system. This approach would be effective in many situations, although it does invariably lead to at least some loss of throughput and increase in thermal background. Any increase in thermal background is detrimental to observations at longer near-infrared wavelengths. We also discuss the importance of considering the effect of ADR when attempting slit-spectroscopy with an AO system.

4.1. Maximum Exposure Times

In the following we adopt the maximum acceptable drift in a single exposure to be 0.25 of the full width half maximum (FWHM) of the diffraction limited core of the science instrument point spread function (PSF), i.e. 1.04 λ/D radian, where λ is the wavelength of the science observation and D is the diameter of the telescope aperture. These calculations were performed for a λ_{eff} of the wavefront sensor of 0.65 μm and a science wavelength of 1.65 μm, which is roughly the middle of H-band. For all of these examples we use the latitude of Mauna Kea observatory in Hawaii ($19\fdg826$ N), but clearly if the sign of the target declination is reversed then these figures would be correct for an observatory at $19\fdg826$ S latitude. In general, an observer closer to the equator will be affected more by ADR than an observer at one of the poles, who will not have to contend with the problems discussed here. All of these calculations assumed zero water vapor. In general reasonable values for the partial pressure of water have little impact on these calculations, but the implications of varying water vapor should be considered if extremely high precision is sought. See Section 2 for further description of these calculations. We are making the IDL code used in this work publicly available for anyone to use to examine the implications of atmospheric differential refraction for their favorite telescope and target. A final note is that nearly all modern telescopes are built on altitude-azimuth mounts which often have a zenith

TABLE 3

DETAILS OF OBSERVATIONS AND RESULTS OF FITTING FOR ATMOSPHERIC DIFFERENTIAL REFRACTION.

Star Name	UT Time Range	Elevation Range	# of images	Best-fit λ_{eff} (μm)[a]
HIP 110a (#1[b])	12:28-13:06	70.°27-68.°68	40	0.611±0.016
HIP 110b (#1[b])	12:28-13:06	70.°27-68.°68	40	0.608±0.014
HIP 110a (#2[b])	13:16-13:55	67.°71-62.°84	41	0.623±0.008
HIP 110b (#2[b])	13:16-13:55	67.°71-62.°84	41	0.623±0.007
HIP 13117a	14:07-14:46	64.°15-68.°98	31	0.735±0.018
HIP 13117b	14:07-14:46	64.°15-68.°98	31	0.730±0.019

[a]See text for details of fitting. This is the effective wavelength of the wavefront sensor of the AO bench when observing this star.

[b]These numbers refer to the first or second sequence of observations on HIP 110.

cone-of-avoidance of up to a few degrees. These cones-of-avoidance are not considered in these calculations, but obviously this will further restrict maximum exposure times on targets that transit near the zenith.

Figure 8 contains contour plots of maximum exposure time in minutes as a function of target declination and hour angle at the start of the exposure. Although few, if any, 4-meter class telescopes are located at sea level, Figure 8a shows such a case. Comparison to Figure 8b, the case of a 4-meter telescope on Mauna Kea, conveys the importance of altitude when considering ADR. In typical near-infrared observations the signal-to-noise ratio (SNR) is often background limited in just a few minutes. So long as the data are background limited, there is no disadvantage to breaking up a long exposure into several shorter exposures. For 4-meter class telescopes this means that ADR will not often be a siginificant problem, except when nearing the readnoise limited regime such as the cases of imaging through narrowband filters or during spectroscopic observations.

We initially encountered the problem of ADR while observing with the Keck II 10-meter telescope, and Figure 8c shows the maximum exposure time for this case. Since maximum exposure time scales nearly linearly with telescope diameter, a wider range of observing strategies are impacted. Again, wideband filter imaging programs will often find their SNR background limited before being ADR limited, but most narrowband

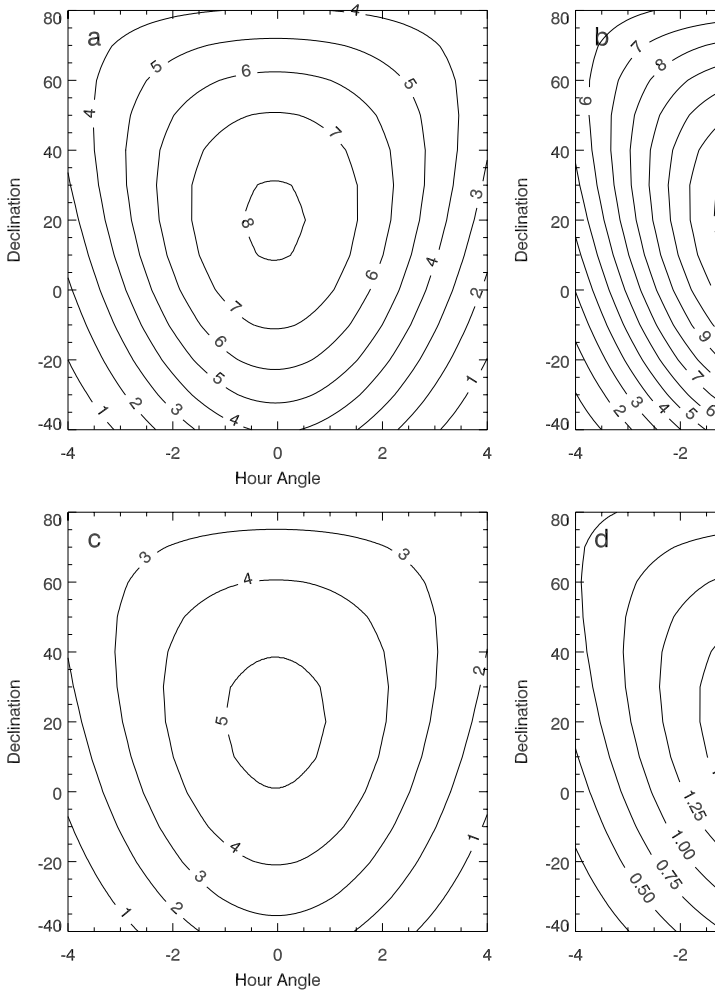

Fig. 8.— Maximum exposure time due to the effect of atmospheric differ
λ_{eff} of the wavefront sensor is 0.65 μm, science observations are at 1.65
maximum allowed image motion is one quarter the FWHM of the diffracti
of 1.65 μm, and that there is no water vapor. (a) is for the case of a 4-mete
of a 4-meter telescope on Mauna Kea, similar to NASA's IRTF 3-meter tel
(c) is for the case of a 10-meter telescope on Mauna Kea, such as the Kec
of a 30-meter telescope on the summit of Mauna Kea. Note that maximu
transit.

imaging and spectroscopic projects will now find that ADR places significantly shorter limits on exposure time than achieving the background limit of the SNR. We discuss another important issue concerning spectroscopic observations in Section 4.3.

Finally, discussions are currently underway about the prospect of building even larger diameter telescopes. The proposals range in telescope diameter up to 100-meters and usually include plans for an AO system. To our knowledge no firm commitments have been made by any group regarding location or size of these proposed telescopes. In Figure 8d we show how important ADR becomes for a 30-meter telescope on Mauna Kea, where maximum exposure times are reduced to a minute or less. Clearly any plans for new, extremely-large telescopes must include a way of correcting for the effect of ADR.

4.2. Partial Correction

The guide star's λ_{eff} on the WFS will often not be known to high precision due either to uncertainties in the spectrum of the star or the shape of the passband of the WFS. Thus, even if an AO system is designed to account for ADR there may still be some image motion due to imperfect knowledge of λ_{eff} on the WFS. The routine *adr_maxexptime2.pro*, included in the electronic version of this paper, calculates the maximum exposure time assuming the AO system is correcting for the effect of ADR using $\lambda_{estimate}$ as λ_{eff} on the WFS while λ_{true} is the actual λ_{eff} on the WFS. When calculating the maximum exposure time, $\lambda_{estimate}$ and λ_{true} are reciprocal, e.g. the maximum exposure time is the same in the case of $\lambda_{true} = 0.6\mu$m and $\lambda_{estimate} = 0.7\mu$m as in the case of $\lambda_{true} = 0.7\mu$m and $\lambda_{estimate} = 0.6\mu$m. In Fig. 9 we show contour plots of maximum exposure time as a function of hour angle and target elevation for a series of $\lambda_{estimate}$ and λ_{true}. We use the parameters of a 10-meter telescope on Mauna Kea, as in Fig. 8c. In each case the error between $\lambda_{estimate}$ and λ_{true} is 0.1μm and the wavelengths examined are 0.5, 0.6, 0.7, 0.8, and 0.9 μm. At shorter wavelengths an 0.1 μm error in the wavelength of correction results in the maximum exposure time being increased by only a factor of less than two. However, at longer wavelengths the same error of 0.1 μm has much less impact and maximum exposure times are increased by a factor of six. This demonstrates that a bluer wavefront sensor passband and/or blue reference source is much less tolerant of errors in the estimate of λ_{eff}. The reason for this significant difference in error tolerance at red and blue visible wavelengths lies in the shape of the curve of refractive index as a function of wavelength, as shown in Fig. 2. The ability to measure the wavefront distortion at a wavelength with a similar index of refraction as the wavelength of observation is one of many reasons that infrared wavefront sensors are appealing.

4.3. Implications for Spectroscopy

The implications of ADR for slit-spectroscopy are somewhat more complicated than for imaging. Along the direction of the slit the issue of image motion is the same, and simply leads to degraded spatial resolution, as happened to the spectrum taken during the images of Titan shown in Fig. 1. However, with spectroscopy one is also concerned with the possibility of biasing the spectrum of the light sent through the slit to the spectrometer. Irrespective of ADR, a narrow slit and/or misalignment of the slit on the target can lead to biased spectra. The easiest way to understand this problem is to imagine a narrow slit centered on the

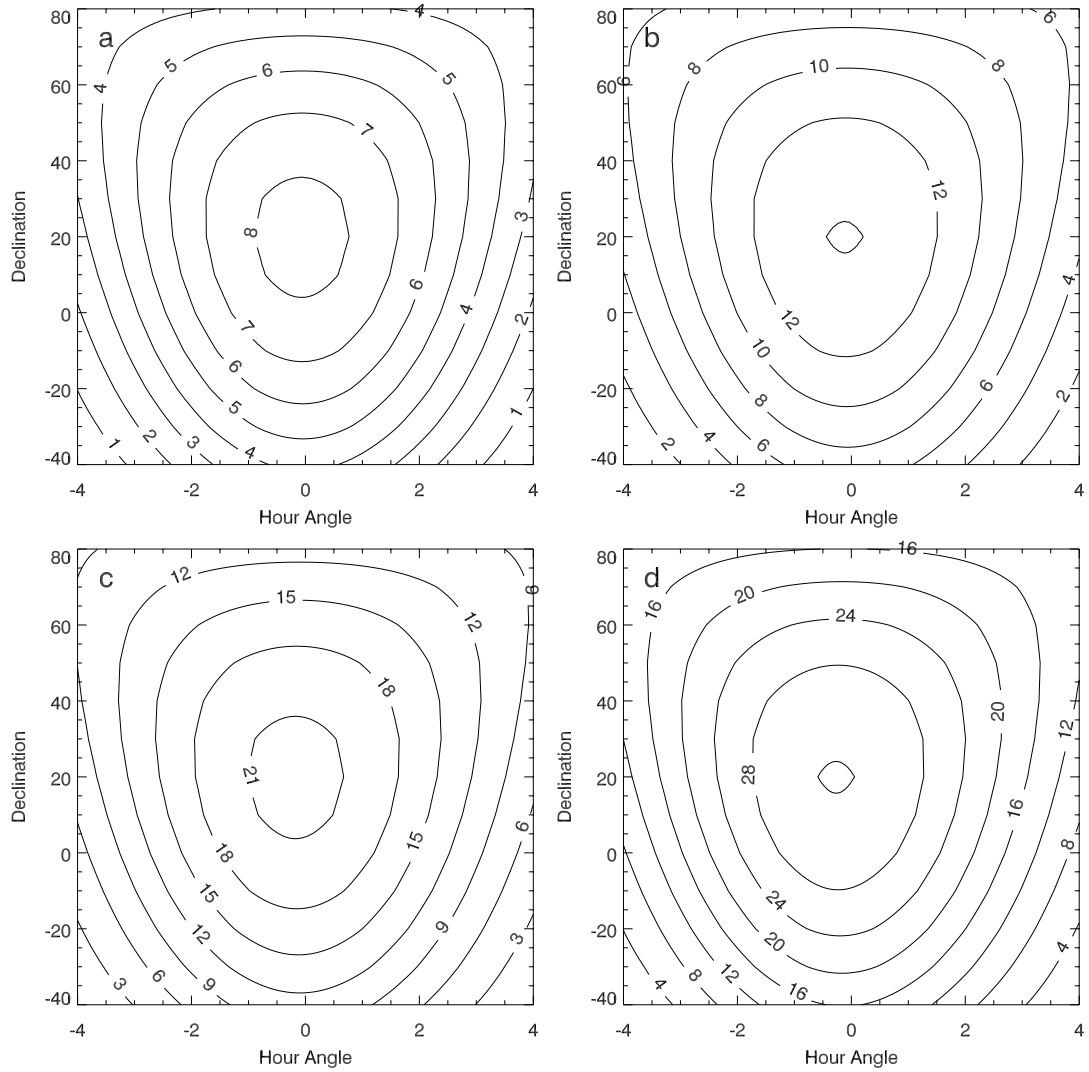

Fig. 9.— Maximum exposure time in the case of a partial correction for differential refraction. All calculations assume that science observations are at 1.65 μm, the telescope diameter is 10 m, observatory latitude is 19.°826 N, and pressure and temperature are typical for Mauna Kea, maximum allowed image motion is one quarter the FWHM of the diffraction limited PSF at the science wavelength of 1.65 μm, and that there is no water vapor. (a) is for $\lambda_{estimate}$ and λ_{true} equal to 0.5 and 0.6 μm, (b) is for 0.6 and 0.7 μm, (c) is for 0.7 and 0.8 μm, and (d) is for 0.8 and 0.9 μm. These plots can be compared with Fig. 8c to see how much maximum exposure time increases between the case of no correction (Fig. 8c) and partial correction.

core of the PSF versus the same slit partway off center. Because the PSF of the bluer end of the spectrum is narrower than the PSF of the red end of the spectrum, the spectrum from the off-center slit will be biased to the red. Residual image motion perpendicular to the slit risks introducing a color bias to the resulting spectrum.

In the case that ADR is not perfectly compensated and image motion results, observers taking spectra should be aware of the choice they are making when orienting their slit. Aligning the slit parallel to the direction of motion due to ADR means degraded spatial resolution along the slit, however this will not introduce any extra color-bias to the spectrum. Aligning the slit perpendicular to this means conserving spatial resolution along the slit, however there is then a risk of introducing a spectral color bias, especially if the target is a point source and the exposure is long. Further, if the target is extended and the slit is oriented perpendicular to the motion of ADR the spatial resolution of the data is also degraded. Ideally for spectral observers ADR would be adequately compensated for by the AO system and the observer would not need to worry about these complications. In the case that the ADR correction is poor or non-existent observers can calculate the direction of motion due to ADR from Equations 10-11, implemented in the routine *adr_rateofmotion.pro*, and decide for themselves the tradeoff between spectral integrity and spatial resolution.

5. Summary

Using theoretical calculations and data from the W.M. Keck II telescope we demonstrate that atmospheric differential refraction (ADR) should be considered when designing and building adaptive optics (AO) systems. We present calculations and IDL code for others to calculate the effect of ADR for their own particular observing parameters. The primary effect of ADR on typical AO observations is to reduce the maximum exposure time possible without significant image blurring. Maximum exposure time decreases approximately linearly with increasing telescope size. Due to the variation of the refractive index of air across visible wavelengths, the maximum exposure time is strongly a function of the effective wavelength of the wavefront sensor. The other important parameters in calculating maximum exposure time are observatory altitude and latitude, target declination and hour angle, and, to a lesser extent during typical near-infrared science observations, the effective wavelength of the science observations. Planning for AO systems on larger (> 10-meter) future telescopes must include consideration for how to compensate for the effect of ADR.

We thank Imke de Pater for her support of this work, James Graham and James Lloyd for the use of their data from August 2001, Eliot Young for the use of the Titan data, and Ray Jayawardhana for his encouragement. We thank the entire staff of the W.M. Keck Observatory, especially David LeMignant, Scott Acton, and Randy Campbell. H.G.R. is supported by a NASA GSRP grant funded through NASA Ames Research Center. This work has been supported in part by the National Science Foundation Science and Technology Center for Adaptive Optics, managed by the University of California at Santa Cruz under cooperative agreement No. AST-9876783. We extend special thanks to those of Hawaiian ancestry on whose sacred mountain we are privileged to be guests. Without their generous hospitality, none of the observations presented herein would have been possible.

REFERENCES

Cohen, J. G. & Cromer, J. 1988, PASP, 100, 1582

Drilling, J. S. & Landolt, A. U. 2000, in Allen's Astrophysical Quantities, 4th edition, ed. Arthur N. Cox. (New York: AIP Press), 381

ESA, 1997, The Hipparcos and Tycho Catalogues (17 volumes), SP-1200

Gavel, D. T., Olivier, S. S., Bauman, B. J., Max, C. E., & Macintosh, B. A. 2000, Proc. SPIE, 4007, 63

Graves, J. E., Northcott, M. J., Roddier, F. J., Roddier, C. A., Potter, D., O'Connor, D. J., Rigaut, F. J., & Chun, M. R. 2000, Proc. SPIE, 4007, 26

Press, W. H., Teukolsky, S. A., Vetterling, W. T., & Flannery, B. P. 1992, Cambridge: University Press, c1992, 2nd ed.,

Rigaut, F. et al. 1998, PASP, 110, 152

Schubert, G. & Walterscheid, R. L. 2000, in Allen's astrophysical quantities, 4th edition, ed. Arthur N. Cox. (New York: AIP Press), 239

Wizinowich, P. et al. 2000, PASP, 112, 315

AAS LaTeX macros v5.0.